

The Heavy Photon Search Test Detector

M. Battaglieri^a, S. Boyarinov^b, S. Bueltmann^c, V. Burkert^b, A. Celentano^a, G. Charles^f, W. Cooper^d, C. Cuevas^b, N. Dashyan^e, R. DeVita^a, C. Desnault^f, A. Deur^b, H. Egriyan^b, L. Elouadrhiri^b, R. Essig^g, V. Fadeyev^h, C. Fieldⁱ, A. Freyberger^b, Y. Gershtein^j, N. Gevorgyan^e, F.-X. Girod^b, N. Grafⁱ, M. Grahamⁱ, K. Griffioen^k, A. Grillo^h, M. Guidal^f, G. Hallerⁱ, P. Hansson Adrian^{i,*}, R. Herbstⁱ, M. Holtrop^l, J. Jarosⁱ, S. Kaneta^b, M. Khandaker^m, A. Kubarovskyⁿ, V. Kubarovsky^b, T. Maruyamaⁱ, J. McCormickⁱ, K. Moffeitⁱ, O. Moreno^h, H. Nealⁱ, T. Nelsonⁱ, S. Niccolai^f, A. Odianⁱ, M. Oriunnoⁱ, R. Paremuzyan^e, R. Partridgeⁱ, S. K. Phillips^l, E. Rauly^f, B. Raydo^b, J. Reichert^j, E. Rindel^f, P. Rosier^f, C. Salgado^m, P. Schuster^o, Y. Sharabian^b, D. Sokhan^p, S. Stepanyan^b, N. Toro^o, S. Uemuraⁱ, M. Ungaro^b, H. Voskanyan^e, D. Walzⁱ, L. B. Weinstein^c, B. Wojtsekhowski^b

^aIstituto Nazionale di Fisica Nucleare, Sezione di Genova e Dipartimento di Fisica dell'Università, 16146 Genova, Italy

^bThomas Jefferson National Accelerator Facility, Newport News, Virginia 23606

^cOld Dominion University, Norfolk, Virginia 23529

^dFermi National Accelerator Laboratory, Batavia, IL 60510-5011

^eYerevan Physics Institute, 375036 Yerevan, Armenia

^fInstitut de Physique Nucléaire, CNRS/IN2P3 and Université Paris Sud, Orsay, France

^gStony Brook University, Stony Brook, NY 11794-3800

^hSanta Cruz Institute for Particle Physics, University of California, Santa Cruz, CA 95064

ⁱSLAC National Accelerator Laboratory, Menlo Park, CA 94025

^jRutgers University, Department of Physics and Astronomy, Piscataway, NJ 08854

^kThe College of William and Mary, Department of Physics, Williamsburg, VA 23185

^lUniversity of New Hampshire, Department of Physics, Durham, NH 03824

^mNorfolk State University, Norfolk, Virginia 23504

ⁿRensselaer Polytechnic Institute, Department of Physics, Troy, NY 12181

^oPerimeter Institute, Ontario, Canada N2L 2Y5

^pUniversity of Glasgow, Glasgow, G12 8QQ, Scotland, UK

Abstract

The Heavy Photon Search (HPS), an experiment to search for a hidden sector photon in fixed target electroproduction, is preparing for installation at the Thomas Jefferson National Accelerator Facility (JLab) in the Fall of 2014. As the first stage of this project, the HPS Test Run apparatus was constructed and operated in 2012 to demonstrate the experiment's technical feasibility and to confirm that the trigger rates and occupancies are as expected. This paper describes the HPS Test Run apparatus and readout electronics and its performance. In this setting, a heavy photon can be identified as a narrow peak in the e^+e^- invariant mass spectrum above the trident background or as a narrow invariant mass peak with a decay vertex displaced from the production target, so charged particle tracking and vertexing are needed for its detection. In the HPS Test Run, charged particles are measured with a compact forward silicon microstrip tracker inside a dipole magnet. Electromagnetic showers are detected in a PbWO₄ crystal calorimeter situated behind the magnet, and are used to trigger the experiment and identify electrons and positrons. Both detectors are placed close to the beam line and split top-bottom. This arrangement provides sensitivity to low-mass heavy photons, allows clear passage of the unscattered beam, and avoids the spray of degraded electrons coming from the target. The discrimination between prompt and displaced e^+e^- pairs requires the first layer of silicon sensors be placed only 10 cm downstream of the target. The expected signal is small, and the trident background huge, so the experiment requires very large statistics. Accordingly, the HPS Test Run utilizes high-rate readout and data acquisition electronics and a fast trigger to exploit the essentially 100% duty cycle of the CEBAF accelerator at JLab.

Keywords: silicon, microstrip, tracking, vertexing, heavy photon, dark photon, electromagnetic calorimeter

1 **1. Introduction**

2 The heavy photon (A'), aka a “hidden sector” or
3 “dark” photon, is a massive gauge boson which couples
4 weakly to electric charge by mixing with the Standard
5 Model photon [1, 2]. Consequently, it can be radiated
6 by electrons and subsequently decay into e^+e^- pairs, al-
7 beit at rates far below those of QED trident processes.
8 Heavy photons have been suggested by numerous be-
9 yond Standard Model theories [3] to explain the discrep-
10 ancy between theory and experiment of the muon’s $g-2$
11 [4], and as a possible explanation of recent astrophysical
12 anomalies, e.g. [5, 6, 7]. Heavy photons couple directly
13 to hidden sector particles with “dark” or “hidden sec-
14 tor” charge; these particles could constitute all or some
15 of the dark matter, e.g. [8, 9]. Current phenomenology
16 highlights the $20 - 1000 \text{ MeV}/c^2$ mass range, and sug-
17 gests that the coupling to electric charge, ϵe , has ϵ in the
18 range of $10^{-3} - 10^{-5}$. This range of parameters makes
19 A' searches viable in medium energy fixed target elec-
20 troproduction [10], but requires large data sets and good
21 mass resolution to identify a small mass peak above the
22 copious QED background. At small couplings, the A'
23 becomes long-lived, so detection of a displaced decay
24 vertex can reject the prompt QED background and boost
25 experimental sensitivity.

26 The HPS experiment [11] is preparing for installation
27 in Hall-B at JLab in the Fall of 2014 to search for heavy
28 photons by directing the 2.2-6.6 GeV CEBAF12 elec-
29 tron beam onto a thin ($0.25\% X_0$) Tungsten target foil.
30 The HPS experiment uses both invariant mass and sec-
31 ondary vertex signatures to search for A' decays into
32 e^+e^- pairs. At CEBAF energies, the A' decay products
33 are boosted along the beam axis with small opening an-
34 gles. For couplings $\epsilon \ll 10^{-3}$, A' decay lengths range
35 from millimeters to tens of centimeters and beyond. Ac-
36 cordingly the tracking detectors cover opening angles
37 down to 15 mrad and are placed just 10 cm downstream
38 of the target.

39 HPS employs a 90 cm long silicon tracking and
40 vertexing detector located inside a dipole magnet to
41 measure momenta and decay vertex positions. A fast
42 PbWO₄ electromagnetic calorimeter downstream of the
43 magnet provides the trigger and electron identification.
44 Both the silicon tracker and the ECal have $\sim\text{ns}$ timing
45 resolution, which eliminates much of the out-of-
46 time background from multiple scattered beam elec-
47 trons. Fast front end electronics and high trigger and

48 data rate capability and the effectively 100% duty cycle
49 of the CEBAF accelerator allows HPS to accumulate the
50 very large statistics needed to be sensitive to the highly
51 suppressed production of heavy photons.

52 The HPS Test Run, using a simplified version of the
53 HPS apparatus, was proposed and approved at JLab as
54 the first stage of HPS. Its purposes included demonstra-
55 ting that the apparatus and data acquisition systems are
56 technically feasible and the trigger rates and occupan-
57 cies to be encountered in electron-beam running are as
58 simulated. Given dedicated running time with electron
59 beams, the HPS Test Run apparatus is capable of search-
60 ing for heavy photons in unexplored regions of parame-
61 ter space. Therefore, key design criteria and require-
62 ments for HPS and the HPS Test Run apparatus are the
63 same:

- 64 • uniform acceptance between 15 and approximately
65 70 mrad in the forward region to catch boosted de-
66 cay products close to the beam,
- 67 • beam passage through the apparatus in vacuum, to
68 eliminate direct interactions with the detector and
69 minimize beam gas interactions,
- 70 • detector components that can survive and effi-
71 ciently operate in a high radiation environment
72 with some localized doses at the 100 Mrad level,
- 73 • high-rate electronics, handling trigger rates up to
74 50 kHz and data rates of 100 MB/s to permanent
75 storage,
- 76 • a flexible, redundant and efficient trigger for select-
77 ing electron and positron pairs, capable of handling
78 rates up to 50 kHz,
- 79 • hit reconstruction efficiency higher than 99% and
80 average track reconstruction efficiency higher than
81 98% for electrons and positrons,
- 82 • 2 ns hit time resolution in the silicon vertex tracker,
- 83 • A' mass resolution of 2.5% or better, which trans-
84 lates to momentum resolution of 4.5% and angular
85 resolution 2 mrad/ $p(\text{GeV}/c)$ for $B=0.5 \text{ T}$,
- 86 • resolution of distance of closest approach to the
87 beam axis less than 250 (100) μm for tracks with
88 0.5 (1.7) GeV/c . This gives a decay length resolu-
89 tion of about 1 mm for a 100 $\text{MeV}/c^2 A'$.
- 90 • PbWO₄ electromagnetic calorimeter energy reso-
91 lution $\Delta E/E \leq 5\%/\sqrt{E}$ and transverse segmentation
92 $\sim 1.5 \text{ cm}$ (Moliere radius in PbWO₄). The energy

*Corresponding author.

Email address: phansson@slac.stanford.edu (P. Hansson Adrian)

resolution for triggering is less stringent because the electrons and positrons of interest are relatively hard. The good segmentation provides good spatial resolution and guarantees minimal shower overlap with background hits.

The HPS Test Run apparatus was installed on April 19, 2012, and ran parasitically in the photon beam of the HDice experiment [12] until May 18. The JLab run schedule precluded any dedicated electron beam running, but the HPS Test Run was allowed an eight hour dedicated photon beam run at the end of scheduled CE-BAF running. During this dedicated period, e^+e^- pairs, produced in a gold foil upstream of the experiment, were studied. With no dedicated electron beam running, it was not possible to search for an A' . However, the final running provided enough data to demonstrate the functionality of the apparatus, document its performance, and explore trigger rates, as shown below.

This paper reviews the HPS Test Run apparatus, documenting the performance of the trigger, data acquisition, silicon tracking and vertex detector, and the electromagnetic calorimeter at, or close to, the level required for the HPS experiment.

2. Detector Overview

The HPS Test Run apparatus was designed to run in Hall B at JLab using the CEBAF 499MHz electron beam at energies between 2.2 and 6.6 GeV and currents between 200 and 600 nA. The overall design of the experiment follows from the kinematics of A' production which typically results in a final state particle within a few degrees of the incoming beam, especially at low $m_{A'}$. Detectors must therefore be placed close to the beam. The intense electron beam enlarges downstream after multiple scattering in the target and electrons which have radiated in the target disperse horizontally in the field of the analyzing magnet. Together they constitute a “wall of flame” which must be completely avoided. Accordingly, the apparatus is split vertically to avoid a “dead zone”, the region within ± 15 mrad of the beam plane. In addition, the beam is transported in vacuum through the tracker to minimize beam-gas interaction backgrounds. Even with these precautions, the occupancies of sensors near the beam plane are high, dominated by the multiple Coulomb scattering of the primary beam, so high-rate detectors, a fast trigger, and excellent time tagging are required to minimize their impact. The trigger comes from a highly-segmented lead-tungstate ($PbWO_4$) crystal calorimeter located just downstream of the dipole magnet.

A rendering of the apparatus installed on the beam line is shown in Figure 1 and an overview of the coverage, segmentation and performance is given in Table 1.

The silicon tracking and vertexing detector for the HPS Test Run, or SVT, resides in a vacuum chamber inside the Pair Spectrometer (PS) dipole magnet in Hall B at JLab. The magnetic field strength was 0.5 T oriented vertically throughout the run. The SVT has five measurement stations, or “layers,” beginning 10 cm downstream of the target. Each layer comprises a pair of closely-spaced silicon microstrip sensors responsible for measuring a single coordinate, or “view”. Introduction of a small (50 or 100 mrad) stereo angle between the two sensors of each layer provides three-dimensional tracking and vertexing throughout the acceptance of the detector. In order to accommodate the dead zone, the SVT is built in two halves that are approximately mirror reflections of one another about the plane of the nominal electron beam. Each layer in one half is supported on a common support plate with independent cooling and readout.

The electromagnetic calorimeter (ECal) is also split into two halves. Each half of the ECal consists of 221 $PbWO_4$ crystals arranged in rectangular formation. There are five rows with 46 crystals in each row except the row closest to the beam plane which has 37. The light from each crystal is read out by an Avalanche Photodiode (APD) glued on the back surface of the crystal. Signals from the APDs are amplified using custom-made amplifier boards before being sent to the data acquisition electronics.

The Data Acquisition system combines two architectures, the Advanced Telecom Communications Architecture (ATCA) based SVT readout system and VME-bus Switched Serial (VXS) based digitization and triggering system for the ECal.

3. The HPS Test Run Beamline

Since an electron beam was unavailable, the HPS Test Run detected the electrons and positrons produced by interactions of the secondary photon beam with a thin foil just upstream of the detectors. The HPS Test Run studied the performance of the detectors and the multiple coulomb scattering of the electrons and positrons. Figure 2 shows the layout of the setup on the beam line. The SVT was installed inside the Hall B pair spectrometer magnet vacuum chamber with the ECal mounted downstream of it. Both the SVT and the ECal were retracted off the beam plane compared to nominal electron

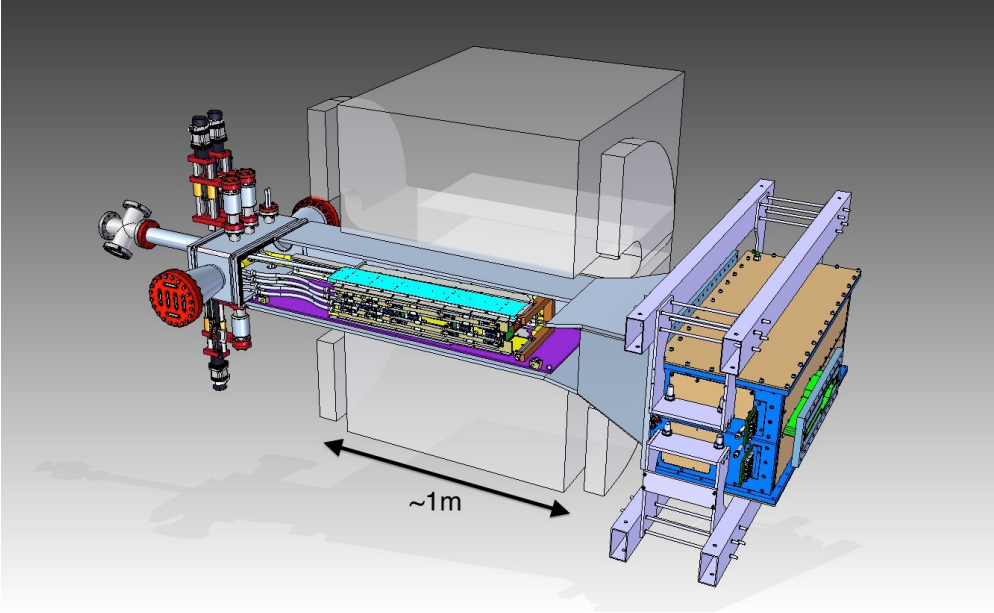


Figure 1: Rendering of the HPS Test Run apparatus installed on the beam line.

Table 1: Overview of the coverage, segmentation and performance of the HPS Test Run detector. The σ_{d_0} is the track impact parameter resolution of the SVT at the nominal electron target position. σ_{pos} is the estimated position resolution perpendicular to the strip direction on the silicon sensors of the SVT.

System	Coverage (mrad)	# channels	ADC (bit)	# layers	Segmentation	Time resolution (ns)	Performance
SVT	$15 < \theta_y < 70$ (5 hits)	12780	14	5 (stereo layers)	$30 \mu\text{m}$ (sense) $60 \mu\text{m}$ (readout) ($\sigma_{pos} \approx 6 \mu\text{m}$)	2.5	$\sigma_{d0,y} \approx 100 \mu\text{m}$ $\sigma_{d0,x} \approx 300 \mu\text{m}$ $\sigma_{d0,z} \approx 1 \text{ mm}$
ECal	$15 < \theta_y < 60$	442	12	1	$1.33 \times 1.33 \text{ cm}^2$ $1.6 \times 1.6 \text{ cm}^2$	4 (trigger)	$\sigma(E)/E \approx 4.5\%/\sqrt{E}$ Ref. [13, 14, 15]

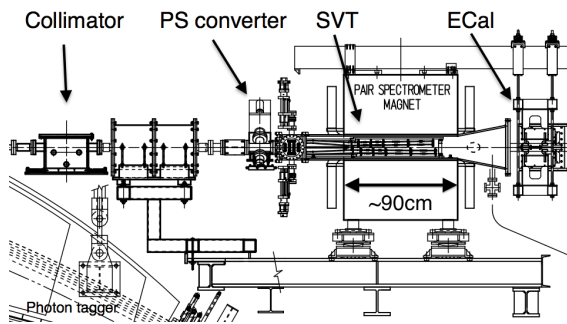


Figure 2: Layout of the HPS parasitic run.

beam running to allow clean passage of the photon beam through the system.

The photon beam was generated in the interaction of 5.5 GeV electrons with a $10^{-4} X_0$ gold radiator located

$\approx 9 \text{ m}$ upstream of the PS. The primary beam and scattered electrons are deflected away from detectors by the dipole magnet of the photon tagging system. During the dedicated HPS Test Run period, the collimated (6.4 mm diameter) photon beam passes through the PS pair converter gold foil and later the HPS system. The PS pair converter was located $\approx 77 \text{ cm}$ upstream of the first layer of the SVT.

Data was taken on three different converter thicknesses with photon fluxes between 0.4 and 1.3×10^8 s at photon energies between 0.55 and 5.5 GeV produced by a 30 to 90 nA electron beam. Data was measured for both polarities of the PS dipole magnet. The photon beam line during the HPS Test Run produced a relatively large number of e^+e^- pairs originating upstream of the converter position. This contribution was measured during data taking with “empty” converter runs,

Converter thickn. (% X_0)	Duration (s)	e^- on radiator (μC)
0	1279	88.1
0.18	2640	193.5
0.45	2149	140.7
1.6	911	24.4

Table 2: Measured integrated currents for the dedicated photon runs.

i.e. removing the converter but with all other conditions the same. The runs taken during the time dedicated to HPS Test Run are summarized in Table 2.

4. Silicon Vertex Tracker

The Silicon Vertex Tracker (SVT) enables efficient reconstruction of charged particles and precise determination of their trajectories. This allows A' decays to be distinguished from background via simultaneous measurements of the invariant mass of e^+e^- decay products and the position of decay vertices downstream of the target.

The design of the SVT is primarily driven by physics requirements and constraints from the environment at the interaction region. The A' decay products have momenta in the range of 0.4-2.0 GeV/c (from a 2.2 GeV beam), so multiple scattering dominates mass and vertexing uncertainties for any possible material budget. The SVT must therefore minimize the amount of material in the tracking volume. The signal yield for long-lived A' is very small, so the rejection of prompt vertices must be exceedingly pure, on the order of 10^{-7} , in order to eliminate all prompt backgrounds. To achieve the required vertexing performance the first layer of the SVT must be placed no more than about 10 cm downstream of the target. At that distance, it is found that the active region of a sensor can be placed as close as 1.5 mm from the center of the beam, defining the 15 mrad “dead zone” mentioned previously, to maximize low-mass A' acceptance with decay products nearly collinear with the beam axis. At the edge of this “dead zone”, the radiation dose approaches 10^{15} electrons/cm²/month, or roughly 3×10^{14} 1 MeV neutron equivalent/cm²/month [16], requiring the sensors to be actively cooled. Meanwhile, very low-energy delta rays from beam-gas interactions would multiply the density of background hits, so the SVT must operate inside the beam vacuum. Finally, in order to protect the sensors, the detector must be movable so that it can be retracted during periods of uncertain beam conditions or beam tuning.

A mass resolution of 2.5% is adequate to extend a bump-hunt search for an A' into virgin territory. For running at 2.2 GeV, this translates into a requirement for track momentum (p) resolution of 4-5% and angular resolution of 2 mrad/ p (GeV/c) [11]. Multiple coulomb scattering dominates both the mass and vertexing uncertainties, relaxing the spatial hit resolution requirement to $< 100 \mu\text{m}$ ($50 \mu\text{m}$) in the bend (non-bend) plane.

High background occupancies, up to 4 MHz/mm² locally, in the region closest to the beam result from beam electrons undergoing multiple scattering in the target. These background hits are rejected by requiring the time reconstruction of each hit to be better than 2 ns.

4.1. Layout

The layout of the SVT is summarized in Table 3 and rendered in Figure 3. Each of the layers is comprised of a pair of closely-spaced silicon microstrip sensors mounted back-to-back to form a module. A 100 mrad stereo angle is used in the first three layers to provide higher-resolution 3D space points for vertexing. Using 50 mrad in the last two layers breaks the tracking degeneracy of having five identical layers and minimizes fakes from ghost hits to improve pattern recognition. Altogether, the SVT has 20 sensors for a total of 12780 readout channels.

Layer	1	2	3	4	5
z from target (cm)	10	20	30	50	70
Stereo angle (mrad)	100	100	100	50	50
Bend res. (μm)	≈ 60	≈ 60	≈ 60	≈ 120	≈ 120
Non-bend res. (μm)	≈ 6	≈ 6	≈ 6	≈ 6	≈ 6
# of sensors	4	4	4	4	4
Dead zone (mm)	± 1.5	± 3.0	± 4.5	± 7.5	± 10.5
Power cons. (W)	6.9	6.9	6.9	6.9	6.9

Table 3: Layout of the SVT.

The SVT is built in two separate halves that are mirror reflections of one another about the plane of the nominal electron beam. Each half consists of five modules mounted on a support plate that provides services to the modules and allows them to be moved as a group relative to the dead zone. The two halves of the tracker are connected to hinges mounted on a C-shaped support just beyond the last layer that defines the nominal spacing between the upper and lower halves of the tracker. A shaft attached to each support plate in front of layer one extends upstream and connects to a linear shift that

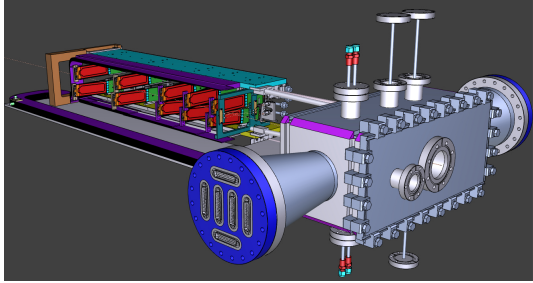


Figure 3: A rendering of the SVT showing the modules on their support plates held by the hinged C-support on the left and the motion levers on the right. The sensors are shown in red and the hybrid readout boards in green. The beam enters from the right through a vacuum box with flanges for services.

transfers motion into the vacuum box through bellows to open and close the two halves around the dead zone. The C-support is mounted to an aluminum baseplate that defines the position of the SVT with respect to the vacuum chamber. Figure 4 shows a photograph of both completed detector halves prior to final assembly.



Figure 4: Both halves of the HPS Test Run SVT after final assembly at SLAC. The cooling manifolds and integrated cable runs are clearly seen.

295

296 4.2. Components

297 The sensors for the SVT are $p+$ -on- n , single-sided,
298 AC-coupled, polysilicon-biased microstrip sensors fab-
299 ricated on $<100>$ silicon and have 30 (60) μm sense
300 (readout) pitch over their $4 \times 10 \text{ cm}^2$ surface. This
301 sensor technology was selected to match the require-
302 ment of $< 1\% X_0$ per layer, single-hit resolution bet-
303 ter than 50 μm and tolerance of a radiation dose of ap-
304 proximately $1.5 \times 10^{14} 1 \text{ MeV}$ neutron equivalent/ cm^2
305 for a six month run. The sensors, produced by Ham-
306 matsu Photonics Corporation, were originally meant

307 for the cancelled Run 2b upgrade of the DØ exper-
308 iment [17] which satisfied the requirement that the tech-
309 nology must be mature and available within the time and
310 budget constraints.

311 Despite having only small spots with very high occu-
312 pancy (up to $4 \text{ MHz}/\text{mm}^2$) closest to the primary beam,
313 the rates are still high and lowering the peak occupancy
314 to approximately 1% for tracking requires a trigger win-
315 dows and hit time tagging of roughly 8 ns. The ECal
316 readout and trigger described in Sec. 5.3 can achieve
317 such resolution. To reach this performance the sen-
318 sors for the SVT are readout by the APV25 ASIC de-
319 veloped for the CMS experiment at CERN [18]. The
320 APV25 can capture successive samples of the shaper
321 output in groups of three at a sampling rate of approx-
322 imately 40 MHz. By fitting the known $CR-RC$ shaping
323 curve to these samples, the initial time of the hit can
324 be determined to a precision of 2 ns for $S/N \approx 25$ [19].
325 For electron beam running, six-sample readout and the
326 shortest possible shaping time (35 ns) is used to best
327 distinguish hits that overlap in time. The APV25 ASICs
328 are hosted on simple FR4 hybrid readout boards, out-
329 side the tracking volume, with a short twisted-pair pig-
330 tail cable to provide power and configuration and signal
331 readout. Along with a single sensor, these are glued
332 to a polyimide-laminated carbon fiber composite back-
333 ing making up a half-module. A window is machined
334 in the carbon fiber leaving only a frame around the pe-
335 riphery of the silicon to minimize material. A 50 μm
336 sheet of polyamide is laminated to the surface of the
337 carbon fiber with 1 mm overhang at all openings to en-
338 sure good isolation between the back side of the sensor,
339 carrying high-voltage bias, and the carbon fiber which
340 is held near ground.

341 The sensor modules for the SVT consist of a pair
342 of identical half-modules, sandwiched back-to-back
343 around an aluminum cooling block at one end and a sim-
344 ilar PEEK spacer block at the other. Figure 5 shows a
345 single module after assembly. The cooling block pro-
346 vides the primary mechanical support for the module as
347 well as cooling via copper tubes pressed into grooves
348 in the plates. The spacer block defines the spacing be-
349 tween the sensors at the far end of the module, stiffens
350 the module structure, and improves the stability of the
351 sensor alignment. The average support material in the
352 tracking volume is approximately $0.06\% X_0$ per double-
353 sided module for a total material budget of 0.7% per
354 layer.

355 The total SVT power consumption budget of about
356 50 W is removed by a water/glycol mixture circulated
357 through a flexible manifold attached to the copper tubes
358 in the cooling blocks. During the HPS Test Run the

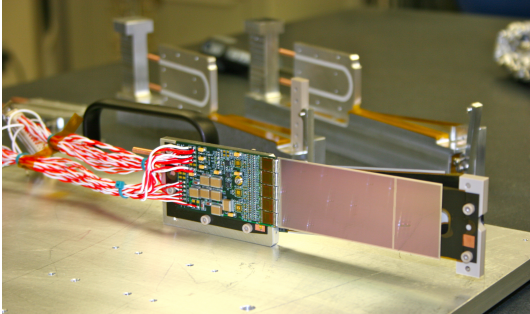


Figure 5: A prototype module assembly (foreground) with the 50 mrad (left) and 100 mrad (right) module assembly fixtures in the background. A pair of cooling blocks and a spacer block can be seen on the fixtures.

sensors were operated at around 23° C. The power consumption is dominated by five APV25 ASICs on each hybrid board consuming approximately 2 W, the radiant heat load is less than 0.5 W per sensor and leakage current is only significant in a small spot after irradiation.

4.3. Production, Assembly and Shipping

Hybrids with APV25 ASICs underwent quick qualification testing and each half-module was run at low temperature ($\approx 5^\circ \text{C}$) and fully characterized for pedestals, gains, noise and time response after assembly. Of 29 half-modules built, 28 passed qualification testing, leaving eight spare modules after completion of the SVT. Only sensors capable of 1000 V bias voltage without breakdown were used. Full-module assembly and mechanical surveys were performed at SLAC before final assembly, testing and shipping of the SVT to JLab. A custom shipping container with nested crates and redundant isolation for shock and vibration was built in order to safely send the partly assembled SVT to JLab. At JLab, the entire SVT was integrated with the full DAQ and the power supplies before moving the module-loaded support plates to Hall B for final mechanical assembly and installation inside of the vacuum chamber.

4.4. Alignment

The SVT was aligned using a combination of optical, laser and touch probe surveys at SLAC and JLab. The optical survey of individual modules with a precision of a few μm was combined with a touch-probe survey of the overall SVT support structure, with 25-100 μm precision, to locate the silicon sensor layers with respect to the support plates and the mechanical survey balls on the base plate. After full assembly and installation

of the SVT at JLab, a mechanical survey of the SVT base plate position inside the pair spectrometer vacuum chamber is used to determine the global position of the SVT with respect to the CEBAF beam line. The resulting survey-based alignment has the position of the silicon sensors correct to within a few hundred microns measured from tracks in the HPS Test Run data. A more sophisticated global track-based alignment technique to reach final alignment precision well below 50 μm is being developed.

5. Electromagnetic Calorimeter

The electromagnetic calorimeter (ECal), installed downstream of the PS dipole magnet, performs two essential functions for the experiment: it provides a trigger signal to select what events to read out from the detector sub-systems and is used to identify electrons and positrons. The technology and design choices are largely driven by the need for a compact forward design covering the SVT A' acceptance and able to measure the energy and positions of electrons and positrons with energy between 0.5-6.5 GeV. It needs granularity and signal readout speed to handle 1 MHz/cm² of electromagnetic background and radiation hardness. Even modest energy resolution is adequate for triggering. HPS requires better energy resolution, $\sigma(E)/E < 5\%/\sqrt{E}$, so that the ECal energy measurement can be used in combination with that from the SVT to improve the overall momentum resolution.

The PbWO₄ crystal inner calorimeter of the CLAS detector [13, 14, 15], in operation since 2005 in Hall B, meets all the requirements set by HPS. The modules from this calorimeter have been subsequently repurposed for HPS.

5.1. Components

The ECal module shown in Figure 6 is based on a tapered 160 mm long PbWO₄ crystal with a 13.3 × 13.3 mm² (16 × 16 mm²) front (rear) face wrapped in VM2000 multilayer polymer mirror film. The scintillation light yield, approximately 120 photons/MeV, is read out by a 5×5 mm² Hamamatsu S8664-55 Avalanche Photodiode (APD) with 75% quantum efficiency glued to the rear face surface using MeltMount 1.7 thermal plastic adhesive. This results in about eight photoelectrons/MeV which needs to be amplified before being fed into the FADC for digitization and processing. The maximum energy deposited in a crystal is expected to be 4.2 GeV which needs to match the input range of the FADC. The relatively low gain of the APD

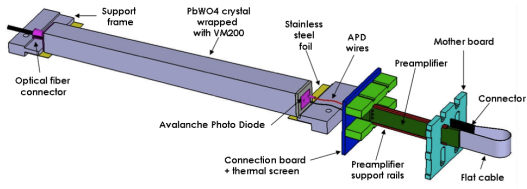


Figure 6: A schematic view of an ECal module.

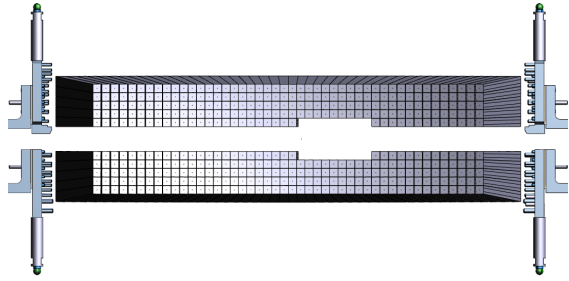


Figure 7: Rendered layout view of the ECal looking downstream.

(~200) was compensated with custom-made preamplifier boards, that provide further amplification to match the 2 V dynamic range of the FADC. With a total noise level of about 10 MeV and a resolution of about 1 ADC count/MeV the ADC resolution fulfills the requirements from HPS.

5.2. Layout

Similar to the SVT, the ECal is built in two separate halves that are mirror reflections of one another about the plane of the nominal electron beam to avoid interfering with the 15 mrad “dead zone”. As shown in Figure 7, the 221 modules in each half, supported by aluminum support frames, are arranged in rectangular formation with five layers and 46 crystals/layer except for the layer closest to the beam where nine modules were removed to allow a larger opening for the outgoing electron and photon beams. Each half was enclosed in a temperature controlled box ($< 1^\circ \text{ F}$ stability and $< 4^\circ \text{ F}$ uniformity) to stabilize the crystal light yield and the operation of the APDs and its preamplifiers. Four printed circuit boards mounted on the backplane penetrated the enclosure and were used to supply the $\pm 5 \text{ V}$ operating voltage for the preamplifiers, 400 V bias voltage to the APDs, and to read out signals from the APDs. Each half of the ECal was divided into 12 bias voltage groups with a gain uniformity of about 20%.

During the HPS Test Run, both halves were held in place by four vertical bars attached to a rail above, placing the front face of the crystals 147 cm from the upstream edge of the magnet, with a 8.7 cm gap between the innermost edge of the crystals in the two halves.

5.3. Signal readout

After a 2:1 signal splitter, 1/3 of an amplified APD signal was fed to a single channel of a JLab flash ADC (FADC) board [20]. 2/3 of the signal was sent to a discriminator module and then to a TDC for a timing measurement. The FADC boards are high speed VXS modules digitizing up to 16 APD signals at 250 MHz and storing samples in 8 μs deep pipelines with 12-bit

resolution. When a trigger is received, the part of the pipeline from five samples before and 30 after the signal which crossed a programmable threshold (for the HPS Test Run this was set to $\approx 70 \text{ MeV}$) are summed and stored in a 17-bit register for readout. In addition a 4 ns resolution timestamp of the threshold crossing is reported in the readout for each pulse. This scheme significantly compresses the data output of the FADC. During offline data analysis, a calibrated pedestal value is subtracted to obtain the actual summed energy. Two 20-slot VXS crates with 14 (13) FADC boards were employed in the HPS Test Run to read out the top (bottom) half of the ECal.

6. Trigger and Data Acquisition

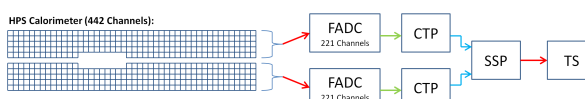
The DAQ system handles acquisition of data from the ECal and SVT sub-detectors with two DAQ architectures. The SVT DAQ is based on Advanced Telecom Communications Architecture (ATCA) hardware while the ECal uses VMEbus Switched Serial (VXS) based hardware. Data from the sub-detectors are only read out when a trigger signal from the trigger system is received.

6.1. Trigger system

The trigger system is designed to select time coincidences of electromagnetic clusters in the top and bottom halves of the ECal which satisfy kinematic conditions satisfied by A' decays and minimize backgrounds. The trigger system needs to be essentially dead-time free, handle rates up to 50 kHz, and supply a trigger signal which jitters $< 8 \text{ ns}$ from the actual event time in order to minimize backgrounds from out-of-time hits in the SVT. Figure 8 shows a schematic overview of each stage of the system. Each channel on the FADC board has an independent data path to send 5-bit pulse energy

512 and 3-bit pulse arrival time information every 32 ns to
 513 a trigger processing board (CTP), which is in the same
 514 crate. The 3-bit pulse arrival time allows the trigger to
 515 know the pulse timing at 4 ns resolution. Contrary to
 516 the readout path described in Sec. 5.3, this energy is a
 517 pedestal-subtracted time-over-threshold sum with pro-
 518 grammable offsets and minimum threshold discrimina-
 519 tor for each channel. With input from all FADC chan-
 520 nels, i.e. one half of the ECal, the CTP performs cluster
 521 finding and calculates cluster energy and timing infor-
 522 mation. The 3x3 fixed-window, highly parallel, FPGA-
 523 based cluster algorithm simultaneously searches for up
 524 to 125 clusters with energy sum larger than the pro-
 525 grammable energy threshold set to about 270 MeV. This
 526 high threshold didn't hurt the trigger rate rate studies
 527 for the HPS Test run since only clusters with high ener-
 528 gies were studied but for HPS this threshold will need to
 529 be lower. Crystals in the fixed-window are included in
 530 the sum if the leading edge of the pulse occurred within
 531 a 32 ns time window to take into account clock skew
 532 and jitter throughout the system. The CTP only accepts
 533 clusters with the locally highest energy 3x3 window to
 534 deal with overlapping and very large clusters. The sub-
 535 system board (SSP) receives the clusters from the top
 536 and bottom half CTP at a maximum of 250MHz and
 537 searches for pairs of clusters in an 8 ns wide coinci-
 538 dence window. The SSP sends triggers to the trigger su-
 539 pervisor (TS), which generates all the necessary signals
 540 and controls the entire DAQ system readout through
 541 the trigger interface units installed in every crate that
 542 participate in the readout process.

543 The trigger system is free-running and driven by the
 544 250 MHz global clock and has essentially zero dead
 545 time at the occupancies expected for HPS. The trigger
 546 supervisor can apply dead time if necessary, for example
 547 on a ‘busy’ or ‘full’ condition from the front-end elec-
 548 tronics. The system is designed to handle trigger rates
 549 above 50 kHz and has a latency set to $\approx 3 \mu\text{s}$ to match



543
 544
 545
 546
 547
 548
 549
 550
 551
 552
 553
 554
 555
 556
 557
 558
 559
 560
 561
 562
 563
 564
 565
 566
 567
 568
 569
 570
 571
 572
 573
 574
 575
 576
 577
 578
 579
 580
 581
 582
 583
 584
 585
 586
 587
 588
 589
 590
 591
 592
 593
 594
 595
 596
 597
 598
 599
 600
 601
 602
 603
 604
 605
 606
 607
 608
 609
 610
 611
 612
 613
 614
 615
 616
 617
 618
 619
 620
 621
 622
 623
 624
 625
 626
 627
 628
 629
 630
 631
 632
 633
 634
 635
 636
 637
 638
 639
 640
 641
 642
 643
 644
 645
 646
 647
 648
 649
 650
 651
 652
 653
 654
 655
 656
 657
 658
 659
 660
 661
 662
 663
 664
 665
 666
 667
 668
 669
 670
 671
 672
 673
 674
 675
 676
 677
 678
 679
 680
 681
 682
 683
 684
 685
 686
 687
 688
 689
 690
 691
 692
 693
 694
 695
 696
 697
 698
 699
 700
 701
 702
 703
 704
 705
 706
 707
 708
 709
 710
 711
 712
 713
 714
 715
 716
 717
 718
 719
 720
 721
 722
 723
 724
 725
 726
 727
 728
 729
 730
 731
 732
 733
 734
 735
 736
 737
 738
 739
 740
 741
 742
 743
 744
 745
 746
 747
 748
 749
 750
 751
 752
 753
 754
 755
 756
 757
 758
 759
 760
 761
 762
 763
 764
 765
 766
 767
 768
 769
 770
 771
 772
 773
 774
 775
 776
 777
 778
 779
 780
 781
 782
 783
 784
 785
 786
 787
 788
 789
 790
 791
 792
 793
 794
 795
 796
 797
 798
 799
 800
 801
 802
 803
 804
 805
 806
 807
 808
 809
 810
 811
 812
 813
 814
 815
 816
 817
 818
 819
 820
 821
 822
 823
 824
 825
 826
 827
 828
 829
 830
 831
 832
 833
 834
 835
 836
 837
 838
 839
 840
 841
 842
 843
 844
 845
 846
 847
 848
 849
 850
 851
 852
 853
 854
 855
 856
 857
 858
 859
 860
 861
 862
 863
 864
 865
 866
 867
 868
 869
 870
 871
 872
 873
 874
 875
 876
 877
 878
 879
 880
 881
 882
 883
 884
 885
 886
 887
 888
 889
 890
 891
 892
 893
 894
 895
 896
 897
 898
 899
 900
 901
 902
 903
 904
 905
 906
 907
 908
 909
 910
 911
 912
 913
 914
 915
 916
 917
 918
 919
 920
 921
 922
 923
 924
 925
 926
 927
 928
 929
 930
 931
 932
 933
 934
 935
 936
 937
 938
 939
 940
 941
 942
 943
 944
 945
 946
 947
 948
 949
 950
 951
 952
 953
 954
 955
 956
 957
 958
 959
 960
 961
 962
 963
 964
 965
 966
 967
 968
 969
 970
 971
 972
 973
 974
 975
 976
 977
 978
 979
 980
 981
 982
 983
 984
 985
 986
 987
 988
 989
 990
 991
 992
 993
 994
 995
 996
 997
 998
 999
 1000
 1001
 1002
 1003
 1004
 1005
 1006
 1007
 1008
 1009
 1010
 1011
 1012
 1013
 1014
 1015
 1016
 1017
 1018
 1019
 1020
 1021
 1022
 1023
 1024
 1025
 1026
 1027
 1028
 1029
 1030
 1031
 1032
 1033
 1034
 1035
 1036
 1037
 1038
 1039
 1040
 1041
 1042
 1043
 1044
 1045
 1046
 1047
 1048
 1049
 1050
 1051
 1052
 1053
 1054
 1055
 1056
 1057
 1058
 1059
 1060
 1061
 1062
 1063
 1064
 1065
 1066
 1067
 1068
 1069
 1070
 1071
 1072
 1073
 1074
 1075
 1076
 1077
 1078
 1079
 1080
 1081
 1082
 1083
 1084
 1085
 1086
 1087
 1088
 1089
 1090
 1091
 1092
 1093
 1094
 1095
 1096
 1097
 1098
 1099
 1100
 1101
 1102
 1103
 1104
 1105
 1106
 1107
 1108
 1109
 1110
 1111
 1112
 1113
 1114
 1115
 1116
 1117
 1118
 1119
 1120
 1121
 1122
 1123
 1124
 1125
 1126
 1127
 1128
 1129
 1130
 1131
 1132
 1133
 1134
 1135
 1136
 1137
 1138
 1139
 1140
 1141
 1142
 1143
 1144
 1145
 1146
 1147
 1148
 1149
 1150
 1151
 1152
 1153
 1154
 1155
 1156
 1157
 1158
 1159
 1160
 1161
 1162
 1163
 1164
 1165
 1166
 1167
 1168
 1169
 1170
 1171
 1172
 1173
 1174
 1175
 1176
 1177
 1178
 1179
 1180
 1181
 1182
 1183
 1184
 1185
 1186
 1187
 1188
 1189
 1190
 1191
 1192
 1193
 1194
 1195
 1196
 1197
 1198
 1199
 1200
 1201
 1202
 1203
 1204
 1205
 1206
 1207
 1208
 1209
 1210
 1211
 1212
 1213
 1214
 1215
 1216
 1217
 1218
 1219
 1220
 1221
 1222
 1223
 1224
 1225
 1226
 1227
 1228
 1229
 1230
 1231
 1232
 1233
 1234
 1235
 1236
 1237
 1238
 1239
 1240
 1241
 1242
 1243
 1244
 1245
 1246
 1247
 1248
 1249
 1250
 1251
 1252
 1253
 1254
 1255
 1256
 1257
 1258
 1259
 1260
 1261
 1262
 1263
 1264
 1265
 1266
 1267
 1268
 1269
 1270
 1271
 1272
 1273
 1274
 1275
 1276
 1277
 1278
 1279
 1280
 1281
 1282
 1283
 1284
 1285
 1286
 1287
 1288
 1289
 1290
 1291
 1292
 1293
 1294
 1295
 1296
 1297
 1298
 1299
 1300
 1301
 1302
 1303
 1304
 1305
 1306
 1307
 1308
 1309
 1310
 1311
 1312
 1313
 1314
 1315
 1316
 1317
 1318
 1319
 1320
 1321
 1322
 1323
 1324
 1325
 1326
 1327
 1328
 1329
 1330
 1331
 1332
 1333
 1334
 1335
 1336
 1337
 1338
 1339
 1340
 1341
 1342
 1343
 1344
 1345
 1346
 1347
 1348
 1349
 1350
 1351
 1352
 1353
 1354
 1355
 1356
 1357
 1358
 1359
 1360
 1361
 1362
 1363
 1364
 1365
 1366
 1367
 1368
 1369
 1370
 1371
 1372
 1373
 1374
 1375
 1376
 1377
 1378
 1379
 1380
 1381
 1382
 1383
 1384
 1385
 1386
 1387
 1388
 1389
 1390
 1391
 1392
 1393
 1394
 1395
 1396
 1397
 1398
 1399
 1400
 1401
 1402
 1403
 1404
 1405
 1406
 1407
 1408
 1409
 1410
 1411
 1412
 1413
 1414
 1415
 1416
 1417
 1418
 1419
 1420
 1421
 1422
 1423
 1424
 1425
 1426
 1427
 1428
 1429
 1430
 1431
 1432
 1433
 1434
 1435
 1436
 1437
 1438
 1439
 1440
 1441
 1442
 1443
 1444
 1445
 1446
 1447
 1448
 1449
 1450
 1451
 1452
 1453
 1454
 1455
 1456
 1457
 1458
 1459
 1460
 1461
 1462
 1463
 1464
 1465
 1466
 1467
 1468
 1469
 1470
 1471
 1472
 1473
 1474
 1475
 1476
 1477
 1478
 1479
 1480
 1481
 1482
 1483
 1484
 1485
 1486
 1487
 1488
 1489
 1490
 1491
 1492
 1493
 1494
 1495
 1496
 1497
 1498
 1499
 1500
 1501
 1502
 1503
 1504
 1505
 1506
 1507
 1508
 1509
 1510
 1511
 1512
 1513
 1514
 1515
 1516
 1517
 1518
 1519
 1520
 1521
 1522
 1523
 1524
 1525
 1526
 1527
 1528
 1529
 1530
 1531
 1532
 1533
 1534
 1535
 1536
 1537
 1538
 1539
 1540
 1541
 1542
 1543
 1544
 1545
 1546
 1547
 1548
 1549
 1550
 1551
 1552
 1553
 1554
 1555
 1556
 1557
 1558
 1559
 1560
 1561
 1562
 1563
 1564
 1565
 1566
 1567
 1568
 1569
 1570
 1571
 1572
 1573
 1574
 1575
 1576
 1577
 1578
 1579
 1580
 1581
 1582
 1583
 1584
 1585
 1586
 1587
 1588
 1589
 1590
 1591
 1592
 1593
 1594
 1595
 1596
 1597
 1598
 1599
 1600
 1601
 1602
 1603
 1604
 1605
 1606
 1607
 1608
 1609
 1610
 1611
 1612
 1613
 1614
 1615
 1616
 1617
 1618
 1619
 1620
 1621
 1622
 1623
 1624
 1625
 1626
 1627
 1628
 1629
 1630
 1631
 1632
 1633
 1634
 1635
 1636
 1637
 1638
 1639
 1640
 1641
 1642
 1643
 1644
 1645
 1646
 1647
 1648
 1649
 1650
 1651
 1652
 1653
 1654
 1655
 1656
 1657
 1658
 1659
 1660
 1661
 1662
 1663
 1664
 1665
 1666
 1667
 1668
 1669
 1670
 1671
 1672
 1673
 1674
 1675
 1676
 1677
 1678
 1679
 1680
 1681
 1682
 1683
 1684
 1685
 1686
 1687
 1688
 1689
 1690
 1691
 1692
 1693
 1694
 1695
 1696
 1697
 1698
 1699
 1700
 1701
 1702
 1703
 1704
 1705
 1706
 1707
 1708
 1709
 1710
 1711
 1712
 1713
 1714
 1715
 1716
 1717
 1718
 1719
 1720
 1721
 1722
 1723
 1724
 1725
 1726
 1727
 1728
 1729
 1730
 1731
 1732
 1733
 1734
 1735
 1736
 1737
 1738
 1739
 1740
 1741
 1742
 1743
 1744
 1745
 1746
 1747
 1748
 1749
 1750
 1751
 1752
 1753
 1754
 1755
 1756
 1757
 1758
 1759
 1760
 1761
 1762
 1763
 1764
 1765
 1766
 1767
 1768
 1769
 1770
 1771
 1772
 1773
 1774
 1775
 1776
 1777
 1778
 1779
 1780
 1781
 1782
 1783
 1784
 1785
 1786
 1787
 1788
 1789
 1790
 1791
 1792
 1793
 1794
 1795
 1796
 1797
 1798
 1799
 1800
 1801
 1802
 1803
 1804
 1805
 1806
 1807
 1808
 1809
 1810
 1811
 1812
 1813
 1814
 1815
 1816
 1817
 1818
 1819
 1820
 1821
 1822
 1823
 1824
 1825
 1826
 1827
 1828
 1829
 1830
 1831
 1832
 1833
 1834
 1835
 1836
 1837
 1838
 1839
 1840
 1841
 1842
 1843
 1844
 1845
 1846
 1847
 1848
 1849
 1850
 1851
 1852
 1853
 1854
 1855
 1856
 1857
 1858
 1859
 1860
 1861
 1862
 1863
 1864
 1865
 1866
 1867
 1868
 1869
 1870
 1871
 1872
 1873
 1874
 1875
 1876

575 the Rear-Transition-Module (RTM), a custom board on 626
576 the back side of the ATCA crate, interfacing the HPS- 627
577 specific readout to the generic DAQ components on the 628
578 COB. A pre-amplifier converts the APV25 differential 629
579 current output to a different voltage output scaled to the 630
580 sensitive range of a 14-bit ADC operating at the system 631
581 clock of 41.667 MHz. The RTM is organized into four 632
582 sections with each section supporting three SVT half- 633
583 module hybrids (15 APV25 ASICs). The RTM also in- 634
584 cludes a 4-channel fiber-optic module and supporting 635
585 logic which is used to interface to the JLab trigger sys- 636
586 tem supervisor. Each section of the RTM is input to a 637
587 DPM which apply thresholds for data reduction and 638
588 organizes the sample data into UDP datagrams. The DPM 639
589 also hosts an I²C controller used to configure and mon- 640
590 itor the APV25 ASICs. A single ATCA crate with two 641
591 COB cards was used, one supporting four DPMs and 642
592 one supporting three DPMs and one DPM that is con- 643
593 figured as the trigger and data transmission module. The 644
594 two COB cards and their DPMs are interconnected with 645
595 a 10 Gb/s switch card [21] which also hosts two 1Gb/s 646
596 Ethernet interfaces to the external SVT DAQ PC.

597 The external PC supports three network interfaces: 647
598 two standard 1 Gb/s Ethernet and one custom low- 648
599 latency data reception card. The first is used for slow 649
600 control and monitoring of the 8 DPM modules and the 650
601 second serves as the interface to the JLAB data acquisi- 651
602 tion system. The third custom low-latency network in- 652
603 terface is used to receive data from the ATCA crate and 653
604 supports a low latency, reliable TTL trigger acknowl- 654
605 edge interface to the trigger DPM. This PC hosts the 655
606 SVT control and monitoring software as well as the 656
607 Read Out Controller application used to interface with 657
608 the JLab DAQ.

609 In order to minimize cable length for the analog 661
610 APV25 output signal the ATCA crate was located ap- 662
611 proximately 1 m from the beam line, next to our cable 663
612 vacuum feed-throughs. Before shielding with lead- 664
613 blankets and borated polyethylene was arranged, we ob- 665
614 served two failures of normally reliable ATCA crate 666
615 power supplies, time-correlated to beam instabilities.

616 Although trigger rates during the HPS Test Run were 667
617 significantly lower, this system was tested at trigger 668
618 rates up to 20 kHz and 50 MB/s. With optimized event 669
619 blocking and improved ethernet bandwidth, together 670
620 with utilizing the overlapping readout and trigger func- 671
621 tionality of the APV25, the system is capable of being
622 read out at 50 kHz trigger rate.

623 6.3. General Data Acquisition and Online Computing

624 Every crate participating in the readout process con- 625
625 tains a Readout Controller (ROC) that collects digitized

information, processes it, and sends it on to the event builder. For the ECal, both VXS crates run ROC applications in a single blade Intel-based CPU module running CentOS Linux OS. For the SVT DAQ, the ROC application runs on the external PC under RHEL. The event builder assembles information from the ROCs into a single event which is passed to the event recorder that writes it to a RAID5-based data storage system capable of handling up to 100 MB/s. The event builder and other critical components run on multicore Intel-based multi-CPU servers. The DAQ network system is a network router providing 10 Gb/s high-speed connection to the JLab computing facility for long-term storage. For the HPS Test Run, both the SVT and ECal ROC had a 1 Gb/s link to the network router.

7. Reconstruction and Performance

While dedicated electron beam was precluded for the HPS Test Run the short dedicated photon beam run allowed the study of some of the key performance parameters for HPS and the trigger rates expected during electron beam running. This section documents the performance and discusses the implications of these results for HPS.

7.1. SVT Performance

For the duration of the HPS Test Run all SVT modules and APV25 chips were configured to their nominal operating points [22] with all sensors reverse-biased at 180 V. The sensors were operated within a temperature range of 20 – 24°C. Approximately 97% of the 12,780 SVT channels were found to be operating normally; the fraction of dead or noisy channels varied from 2.4% to 4.7% throughout the HPS Test Run. Most of these losses were due to 2-4 misconfigured APV25 ASICs, a known noisy half-module and problems in two particular APV25 ASICs.

7.1.1. Cluster and Hit Reconstruction

Track reconstruction in the SVT puts stringent requirement on the clustering and hit reconstruction. The multiple scattering in the tracking material dominates the uncertainty in the track parameter estimation and effectively determines the roughly 50 μm (200 μm) requirement on the spatial hit resolution in the non-bend (bend) plane. The high occupancy due to multiple scattered beam electrons in the target close to the beam requires a hit time resolution of 2 ns to efficiently reject out-of-time hits in HPS. Both the hit time, based on a

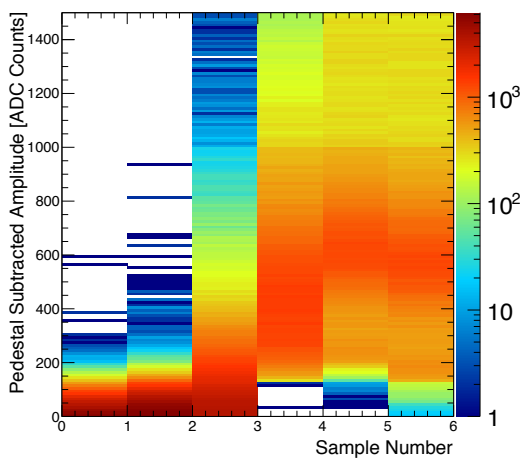


Figure 11: Accumulation of six pedestal-subtracted samples from individual SVT channels associated with hits on tracks.

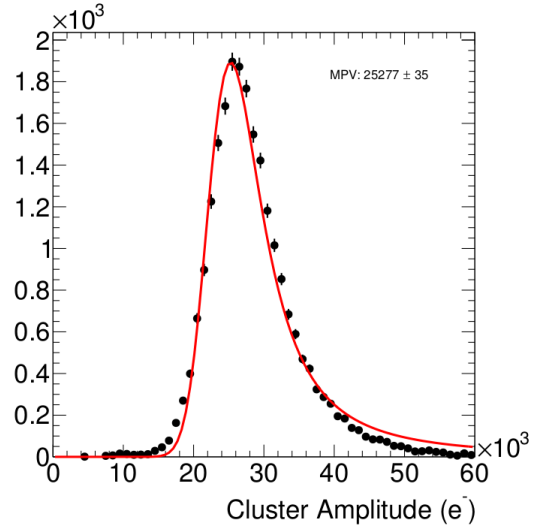


Figure 12: The cluster charge distribution for hits associated with a track follow the characteristic Landau shape.

fit to the APV25 ASIC pulse shape, and the spatial position reconstruction rely on having S/N around 25 for the sensors used in HPS.

After a trigger is received, the amplitude of every APV25 is sampled and digitized in the six consecutive time bins associated with the trigger time. A data reduction algorithm is applied requiring three out of six samples to be above two times the noise level and that the third sample is larger than the second or that the fourth sample is larger than the third. The typical, pedestal subtracted, pulse shape obtained is shown in Figure 11. As the figure demonstrates, the SVT was well timed-in to the trigger with the rise of the pulse at the 3rd sampling point. In order to find the time, t_0 , and amplitude of each hit, the six samples from each channel are fitted to an ideal $CR - RC$ function. Note that in the HPS Test Run the APV25 ASICs were operating with a 50 ns shaping time. These hits are passed through a simple clustering algorithm which forms clusters by grouping adjacent strips with the position of a cluster on the sensor determined by the amplitude-weighted mean. With a linear gain up to ≈ 3 MIPs, the cluster charge for hits associated with a track follow the characteristic Landau shape, see Figure 12. A noise level between $1.1 - 1.5 \times 10^3$ electrons was established through multiple calibration runs giving a signal to noise ratio of 21 – 25, in line with the requirement for HPS. Radioactive source tests were used to provide the absolute charge normalization. After clustering hits on a sensor, the hit time for each cluster is computed as the

amplitude-weighted average of the individually fitted t_0 on each channel. The t_0 resolution is studied by comparing the cluster hit time with the average of all cluster hit times on the track shown in Figure 13. After correcting for offsets from each sensor (time-of-flight and clock phase) and accounting for the correlation between the t_0 and track time, the extracted t_0 resolution is 2.6 ns. This is somewhat worse than the approximately 2 ns resolution expected for S/N=25 which we attribute to the true pulse shape differing from our idealized fit function which will be improved in the future [23]. Reducing the APV25 ASIC pulse shaping time to 35 ns will also improve time resolution. These results show that we can operate with the six sample readout mode of the APV25 chip and achieve time resolution adequate for pileup rejection during electron running in HPS.

Good agreement was obtained between observed and simulated occupancies after taking into account dead or noisy channels. The hit reconstruction efficiency was estimated by measuring the number of good tracks with a hit close to the interpolated position on a given sensor that was excluded from the track fit. Tracks which intersect regions with known bad channels or pass very close to the edge region were excluded. The hit reconstruction efficiency, see Figure 14, was measured to be above 98% and fairly uniform across the SVT.

The spatial resolution of similar microstrip sensors is well established by test beam data, against which the charge deposition model in the simulation is validated.

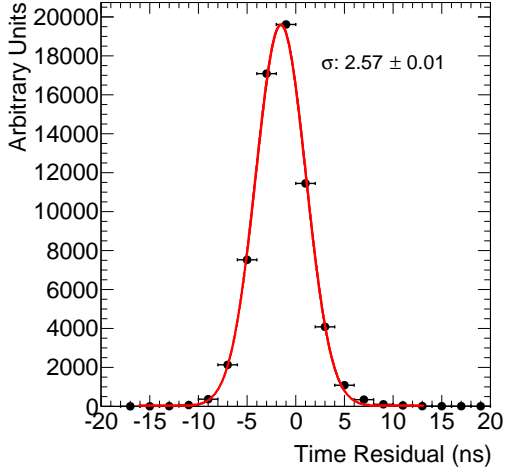


Figure 13: The residual of individual cluster times with the average of all clusters on the track.

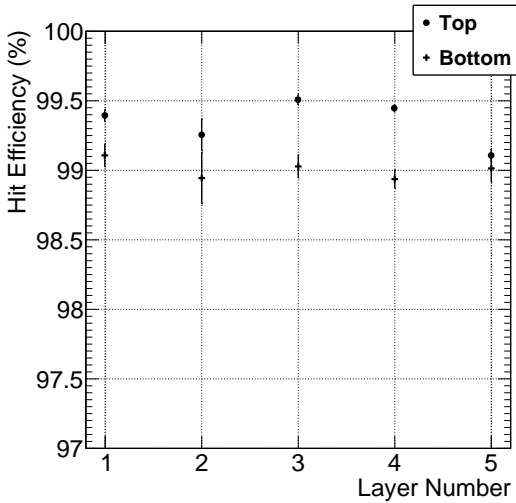


Figure 14: The hit reconstruction efficiency as a function of detector layer.

This resolution can be parameterized as a function of the total signal to single-strip noise and the crossing angle of tracks through the sensor. The single-hit resolution for charged particles with signal-to-noise ratio above 20, as demonstrated here, is relatively constant at approximately $6 \mu\text{m}$ for tracks that enter approximately normal to the sensors as in HPS. This resolution is significantly better than the requirement for reaching the mass and vertex resolutions required for HPS.

7.1.2. Momentum and Vertexing Resolution

Good track reconstruction performance is crucial to HPS. Simulations show that track momentum resolution of 4-5% is needed to achieve the desired A' mass resolution. The precise reconstruction of the production vertex to reject prompt QED background requires impact parameter resolutions between $100-250 \mu\text{m}$ for tracks between $0.5-1.7 \text{ GeV}/c$. These key performance parameters were studied in the HPS Test Run by selecting e^+e^- pairs from photon conversions. Pairs of oppositely charged tracks, one in the top and one in the bottom half of the SVT, with momentum larger than $400 \text{ MeV}/c$ were selected and basic distributions of pair production kinematics were studied. The kinematics are relatively well reproduced as shown in Figure 15.

The expected momentum resolution from simulation is between 4-5% for tracks in the momentum range of the HPS Test Run. By comparing the shapes of the kinematic distributions for data and simulation, we estimate an agreement with the nominal scale and resolution to within 10%.

In the HPS Test Run, as well as in electron running with HPS, the dominant source of uncertainty in the tracking and vertexing is multiple Coulomb scattering. For the vertexing performance the foremost difference between the HPS Test Run and HPS is that the HPS Test Run target is 67 cm further upstream, so tracks must be extrapolated nearly eight times as far as in HPS, giving almost collinear tracks in the detector. The increased lever arm over which tracks are extrapolated worsens the resolution up to a factor of eight (depending on momentum) compared to what is achieved at the nominal electron target position for HPS. Figure 16 shows the horizontal and vertical positions of the extrapolated track at the converter position. While residual alignments show small shifts, the good agreement between data and simulated events of the widths indicates a good understanding of the material budget and distribution in the SVT. Having the dominant contribution to the vertex resolution approximately right demonstrates that the

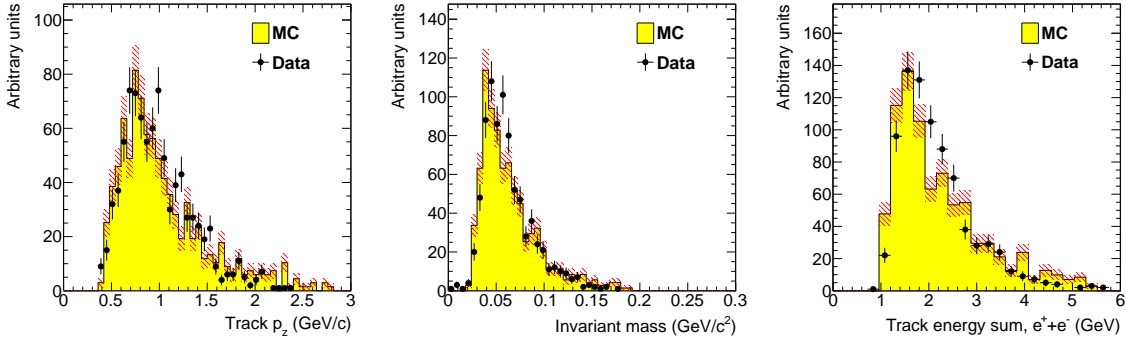


Figure 15: Kinematic distributions for e^+e^- pairs selected by opposite charged tracks in the top and bottom half of the tracker: track momentum in the top half of the SVT (left), invariant mass (middle) and the sum of the track energy for the pair (right).

781 Gaussian part of the vertex resolution in HPS, with a
782 target at 10 cm, will be as calculated.

7.2. ECal Performance

783 During the HPS Test Run 385 out of 442 modules
784 (87%) were used in offline reconstruction, 39 modules
785 were disabled or not read out (no FADC channel avail-
786 able, no APD bias voltage or masked out due to exces-
787 sive noise) and 18 were masked offline due to noise.

788 The integrated pulse of each FADC channel was con-
789верted to energy by subtracting a pedestal and applying
790 a conversion factor to convert ADC counts to energy.
791 The pedestals are measured using special runs where
792 each trigger records 100 samples of signals from the
793 APDs with 4 ns between each sample. The pedestals
794 were extracted from the part of the window before the
795 actual hit in the calorimeter. Modules with signal above
796 the threshold are clustered using a simple algorithm
797 similar to the one deployed for the trigger (see Sec. 6.1).
798 Due to the high effective crystal readout threshold of
799 73 MeV the average number of crystals in a cluster
800 was only about three and the simple clustering algo-
801 rithm worked well for reconstruction of the detected
802 shower energy. An average noise level of approximately
803 15 MeV per crystal was measured in special pedestal
804 runs. The high crystal noise level and effective threshold
805 didn't hurt the trigger rate studies in the HPS Test Run
806 as clusters with high energy were used for the analysis.
807 For HPS the noise level and threshold will be lowered
808 to improve energy resolution and to allow triggering on
809 cosmic rays to improve calibration.

810 The ratio of the ECal cluster energy E to the momen-
811 tum p of a matched track in the SVT was used to de-
812 termine the conversion factors from ADC counts to en-
813 ergy. To compare data and simulation, all inoperable or
814 noisy channels in the SVT and ECal were disabled in

815 both data and simulation so that any efficiency or bias
816 that affect the data should be reflected in the simulation.
817 Iteratively, conversion coefficients for each crystal were
818 adjusted until the E/p ratio in data and simulation were
819 similar. The distribution of the E/p ratio in data and
820 simulation are compared in Figure 17. The peak of the
821 distribution, at $E/p \sim 0.7$, gives the sampling fraction
822 of the ECal, the fraction of the incident particle energy
823 measured in the cluster. The width of the distribution
824 indicates the energy resolution, which is worse than the
825 required $4.5\%/\sqrt{E}$ for HPS due to high thresholds. The
826 width in data is greater than that in simulation due to
827 non-uniformity of the calibration of different parts of
828 the ECal.

829 The A' trigger in HPS is relatively insensitive to the
830 energy of the clusters and this level of performance
831 would be adequate. However, improvements are needed
832 to achieve the expected energy resolution in HPS ($< 4.5\%/\sqrt{E}$). The noise and thresholds need to be
833 closer to 10 MeV and a more elaborate calibration tech-
834 nique needs to be employed to suppress the large tails
835 in the E/p distribution further. In addition, the fraction
836 of working channels needs significant improvement.

7.3. Trigger Performance

837 As described above in Sec. 6, the energy from each
838 crystal is determined slightly differently in the trigger
839 and in the readout. The trigger performance was studied
840 by simulating the trigger for each event and comparing
841 to how the events were actually triggered. To eliminate
842 trigger bias, we use a tag and probe method: to study the
843 trigger performance in one half of the ECal, we select
844 events which triggered the other half and where there
845 was exactly one probe cluster in the ECal half under
846 study. We then measure trigger efficiency as the frac-
847 tion of tagged events that fired the trigger in the probe
848

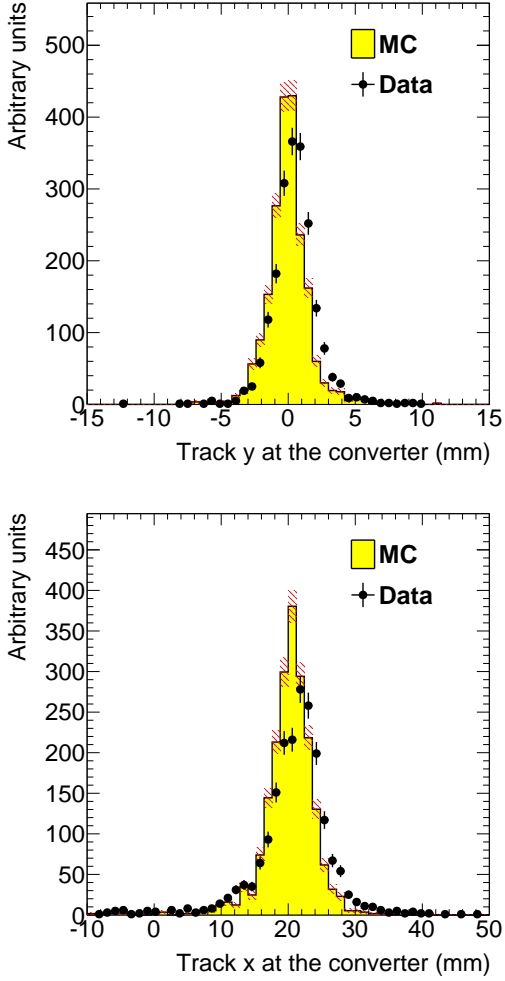


Figure 16: Vertical (top) and horizontal (bottom) extrapolated track position at the converter position taking into account the measured fringe field.

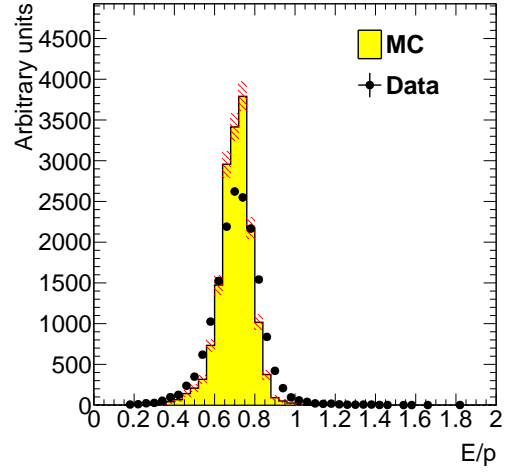


Figure 17: The ECal energy over track momentum ratio (E/p) comparing data and simulation for single cluster triggers in the top half of the ECal.

851 half as a function of the probe cluster energy, shown
 852 in Figure 18. The trigger turn-on is slow and reaches
 853 an uneven plateau at about 700 MeV for two reasons;
 854 gain variations between different crystals lead to the
 855 threshold variations and the nonlinearity of the time-
 856 over-threshold integral means that the effective thresh-
 857 old is higher for clusters that span multiple crystals. The
 858 effective trigger threshold is therefore dependent on po-
 859 sition and energy of the particle as well as cluster multi-
 860 plicity. For HPS the trigger cluster threshold will be set
 861 at a lower value.

862 As a cross-check we simulate the FADC trigger path
 863 by converting from readout hits (with fixed-size win-
 864 dows integration) to trigger hits (time-over-threshold in-
 865 tegration). The CTP clustering algorithm and the trigger
 866 decision from the SSP are simulated before we com-
 867 pare the trigger decision and trigger time to what was
 868 reported by the actual trigger. For every event, the trig-
 869 ger reports the trigger decision as a bit mask (top half,
 870 bottom half or both) and the time the trigger fired. The
 871 turn-on from the trigger threshold was measured to be
 872 1280 in units of ADC counts as expected. The threshold
 873 was not perfectly sharp because of uncertainties in the
 874 conversion from readout to trigger hits described above,
 875 but based on comparisons with simulation we found that
 876 the trigger worked exactly as specified.

877 7.4. Trigger Rate Comparisons

878 Trigger rates observed in the HPS Test Run are dom-
 879 inated by e^+e^- pairs produced in the converter. In sim-

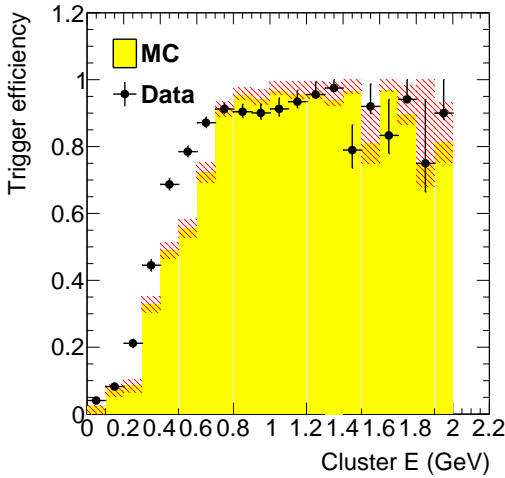


Figure 18: Trigger efficiency in both halves of the ECal for data and simulation as a function of cluster energy.

Converter (% X_0)	1.60	0.45	0.18
EGS5	1162 ± 112	255 ± 28	94 ± 17
Geant4	2633 ± 250	371 ± 38	114 ± 18
Observed	1064 ± 2	196 ± 1	92 ± 1

Table 4: Observed and predicted event rate (in Hz) normalized to 90 nA for three different converter thicknesses. The uncertainty on the prediction includes systematic uncertainties from ECal alignment, background normalization, beam current normalization and limited statistics in the simulation.

ulated events, the rate of triggers depend on the modeling of the pairs' angular distribution and the subsequent multiple Coulomb scattering in the converter. Rates from different converter thicknesses are used to study the varying multiple Coulomb scattering contribution (pair production angular distribution is constant), and are compared with Geant4 [24] standard multiple scattering model and EGS5 [25]. Restricting to a well calibrated region of the ECal and to clusters with energy above the trigger turn-on, we see agreement with the rates predicted by the EGS5 simulation program after subtracting the "no converter" background , see Table 4. This gives further confidence that the dominant source of background occupancy for HPS, multiple Coulomb scattered beam electrons, is well described.

8. Summary and Outlook

The HPS Test Run experiment, using a simplified version of the apparatus planned for the full HPS experiment in a parasitic photon beam, demonstrated the

feasibility of the detector technologies proposed for the silicon vertex tracker, electromagnetic calorimeter, and data acquisition systems. Performance from each of these subsystems has been shown to be adequate to conduct the full experiment successfully with some identified improvements. Studies of multiple Coulomb scattering tails of electrons and positrons from photon conversions further backs expectations from simulation, giving credence to estimates of the detector backgrounds expected in electron beam running for HPS.

9. Acknowledgements

The authors are grateful for the support from Hall B at JLab and especially the Hall B engineering group for support during installation and decommissioning. They also would like to commend the CEBAF personnel for good beam performance, especially the last few hours of operating CEBAF6. The tremendous support from home institutions and supporting staff also needs praise from the authors.

This work has been supported by the US Department of Energy, the National Science Foundation, French Centre National de la Recherche Scientifique and Italian Istituto Nazionale di Fisica Nucleare. Rouven Essig is supported in part by the Department of Energy Early Career research program DESC0008061 and by a Sloan Foundation Research Fellowship. Authored by Jefferson Science Associates, LLC under U.S. DOE Contract No. DE-AC05-06OR23177.

References

- [1] B. Holdom, Two U(1)'s and Epsilon Charge Shifts, Phys.Lett. B166 (1986) 196.
- [2] P. Galison, A. Manohar, TWO Z's OR NOT TWO Z's?, Phys.Lett. B136 (1984) 279.
- [3] R. Essig, J. A. Jaros, W. Wester, P. H. Adrian, S. Andreas, et al. (Report of the Community Summer Study 2013 (Snowmass) Intensity Frontier New, Light, Weakly-Coupled Particles subgroup), Dark Sectors and New, Light, Weakly-Coupled Particles, 2013. URL: <http://arxiv.org/abs/arXiv:1311.0029>.
- [4] M. Pospelov, Secluded U(1) below the weak scale, Phys.Rev. D80 (2009) 095002.
- [5] O. Adriani, et al. (PAMELA Collaboration), An anomalous positron abundance in cosmic rays with energies 1.5-100 GeV, Nature 458 (2009) 607–609.
- [6] M. Ackermann, et al. (Fermi LAT Collaboration), Measurement of separate cosmic-ray electron and positron spectra with the Fermi Large Area Telescope, Phys.Rev.Lett. 108 (2012) 011103.
- [7] M. Aguilar, et al. (AMS Collaboration), First Result from the Alpha Magnetic Spectrometer on the International Space Station: Precision Measurement of the Positron Fraction in Primary Cosmic Rays of 0.5350 GeV, Phys.Rev.Lett. 110 (2013) 141102.

- 952 [8] N. Arkani-Hamed, D. P. Finkbeiner, T. R. Slatyer, N. Weiner, A
 953 Theory of Dark Matter, Phys.Rev. D79 (2009) 015014.
- 954 [9] M. Pospelov, A. Ritz, Astrophysical Signatures of Secluded
 955 Dark Matter, Phys.Lett. B671 (2009) 391–397.
- 956 [10] J. D. Bjorken, R. Essig, P. Schuster, N. Toro, New Fixed-Target
 957 Experiments to Search for Dark Gauge Forces, Phys.Rev. D80
 958 (2009) 075018.
- 959 [11] A. Grillo, et al. (HPS Collaboration), Heavy Photon Search
 960 Proposal, 2010. URL: https://confluence.slac.stanford.edu/download/attachments/86676777/HPSProposal-FINAL_Rev2.pdf.
- 961 [12] A. Sandorfi, et al., 2012. URL: http://www.jlab.org/exp_prog/proposals/06/PR06-101.pdf.
- 962 [13] F.-X. Girod, M. Garon (CLAS), Inner calorimeter in clas/dvcs
 963 experiment, CLAS-Note 2005-001 (2005).
- 964 [14] R. Niyazov, S. Stepanyan (CLAS), Clas/dvcs inner calorimeter
 965 calibration, CLAS-Note 2005-021 (2005).
- 966 [15] F.-X. Girod (Universite de Strasbourg), 2006. URL: <http://www.jlab.org/Hall-B/general/thesis/fxgirrod.pdf>.
- 967 [16] I. Rashevskaya, S. Bettarini, G. Rizzo, L. Bosisio, S. Dittongo,
 968 et al., Radiation damage of silicon structures with electrons of
 969 900-MeV, Nucl. Instrum. Meth. A485 (2002) 126–132.
- 970 [17] D. S. Denisov, S. Soldner-Rembold, D0 Run IIB Silicon Detec-
 971 tor Upgrade: Technical Design Report (2001).
- 972 [18] M. French, L. Jones, Q. Morrissey, A. Neviani, R. Turchetta,
 973 et al., Design and results from the APV25, a deep sub-micron
 974 CMOS front-end chip for the CMS tracker, Nucl.Instrum.Meth.
 975 A466 (2001) 359–365.
- 976 [19] M. Friedl, C. Irmler, M. Pernicka, Readout of silicon strip detec-
 977 tors with position and timing information, Nucl.Instrum.Meth.
 978 A598 (2009) 82–83.
- 979 [20] H. Dong, et al., Integrated tests of a high speed VXS switch
 980 card and 250 MSPS flash ADCs, 2007. doi:[10.1109/NSSMIC.2007.4436457](https://doi.org/10.1109/NSSMIC.2007.4436457).
- 981 [21] R. Larsen, Emerging New Electronics Standards for Physics,
 982 Conf.Proc. C110904 (2011) 1981–1985.
- 983 [22] L. Jones, APV25-S1: User guide version 2.2, RAL Microelec-
 984 tronics Design Group, 2011.
- 985 [23] M. Friedl, C. Irmler, M. Pernicka, Obtaining exact time infor-
 986 mation of hits in silicon strip sensors read out by the APV25
 987 front-end chip, Nucl. Instrum. Meth. A572 (2007) 385 – 387.
- 988 [24] S. A. et al., GEANT4 - a simulation toolkit, Nucl.Instrum.Meth.
 989 A506 (2003) 250 – 303.
- 990 [25] H. Hirayama, Y. Namito, A. Bielajew, S. Wilderman, W. Nelson,
 991 The EGS5 Code System, 2005.
- 992
- 993
- 994
- 995
- 996